## Title

Integrative transcriptomics and cell systems analyses reveal protective pathways controlled by Igfbp-3 in anthracycline-induced cardiotoxicity



## Journal

The FASEB Journal, 37(6)

## ISSN

0892-6638

## Authors

Chen, Junjie
Chapski, Douglas J
Jong, Jeremy
et al.

## Publication Date

2023-06-01

## DOI

10.1096/fj.202201885rr

Peer reviewed

HHS Public Access

Author manuscript

*FASEB J.* Author manuscript; available in PMC 2024 June 01.

Published in final edited form as:

*FASEB J.* 2023 June ; 37(6): e22977. doi:10.1096/fj.202201885RR.

# Integrative Transcriptomics and Cell Systems Analyses Reveal Protective Pathways Controlled by Igfbp-3 in Anthracycline-Induced Cardiotoxicity

**Junjie Chen**[1], **Douglas J. Chapski**[2], **Jeremy Jong**[3], **Jerome Awada**[3], **Yijie Wang**[3], **Dennis J. Slamon**[4,5], **Thomas M. Vondriska**[1,2,3,6,7], **René R. Sevag Packard**[1,3,5,6,7,8,9,10]

[1]Molecular, Cellular, and Integrative Physiology Program, College of Letters and Science, and David Geffen School of Medicine, University of California, Los Angeles, CA

[2]Department of Anesthesiology & Perioperative Medicine, David Geffen School of Medicine, University of California, Los Angeles, CA

[3]Division of Cardiology, Department of Medicine, David Geffen School of Medicine, University of California, Los Angeles, CA

[4]Division of Hematology & Oncology, Department of Medicine, David Geffen School of Medicine, University of California, Los Angeles, CA

[5]Jonsson Comprehensive Cancer Center, University of California, Los Angeles, CA

[6]Department of Physiology, David Geffen School of Medicine, University of California, Los Angeles, CA

[7]Molecular Biology Institute, University of California, Los Angeles, CA

[8]Ronald Reagan UCLA Medical Center, Los Angeles, CA

[9]Veterans Affairs West Los Angeles Medical Center, Los Angeles, CA

[10]California NanoSystems Institute, University of California, Los Angeles, CA

## Abstract

Anthracyclines such as doxorubicin (Dox) are effective chemotherapeutic agents, however their use is hampered by subsequent cardiotoxicity risk. Our understanding of cardiomyocyte protective pathways activated following anthracycline-induced cardiotoxicity (AIC) remains incomplete. Insulin-like growth factor binding protein (IGFBP) 3 (Igfbp-3), the most abundant IGFBP family member in the circulation, is associated with effects on the metabolism, proliferation, and survival of various cells. Whereas Igfbp-3 is induced by Dox in the heart, its role in AIC is ill-defined. We investigated molecular mechanisms as well as systems-level transcriptomic

**Corresponding author:** René R. Sevag Packard, 10833 Le Conte Ave., CHS Building Room 17-054A, Los Angeles, CA 90095. rpackard@mednet.ucla.edu. Tel: 617-671-9018.

Author contributions

Conceptualization, J.C. and R.R.S.P.; Methodology, J.C., D.J.C., D.J.S., T.M.V. and R.R.S.P.; Investigation, J.C., D.J.C., J.J., Y.W., J.A.; Formal Analysis, J.C., D.J.C., J.J. and J.A.; Writing—Original Draft, J J.C. and R.R.S.P.; Writing—Review & Editing, J.C., D.J.C., T.M.V. and R.R.S.P.; Funding Acquisition, R.R.S.P.; Resources, D.J.S., T.M.V. and R.R.S.P.; Supervision, T.M.V. and R.R.S.P.

Conflict of interest statement

The authors declare no conflicts of interest.

consequences of manipulating Igfbp-3 in AIC using neonatal rat ventricular myocytes and human induced pluripotent stem cell-derived cardiomyocytes. Our findings reveal that Dox induces the nuclear enrichment of Igfbp-3 in cardiomyocytes. Furthermore, Igfbp-3 reduces DNA damage, impedes topoisomerase IIb expression (Top2β) which forms Top2β -Dox-DNA cleavage complex leading to DNA double-strand breaks (DSB), alleviates detyrosinated microtubule accumulation – a hallmark of increased cardiomyocyte stiffness and heart failure – and favorably affects contractility following Dox treatment. These results indicate that Igfbp-3 is induced by cardiomyocytes in an effort to mitigate AIC.

## Graphical Abstract

Doxorubicin induces Igfbp-3 upregulation and nuclear translocation in cardiomyocytes. Igfpb-3 overexpression impedes Top2β expression and decreases Dox induced dsDNA break. In parallel, the heart failure markers *Nppa* and *Nppb* are significantly downregulated, while *Cpt1b, Idh3g,* and *Ndufv1*, which positively regulate cellular metabolic activity are significantly upregulated by Igfbp-3 overexpression. Functionally, Igfbp-3 knockdown leads to contractile dysfunction in iPSC-CM after Dox treatment, associated with upregulation of tubulin family genes and accumulation of detyrosinated tubulin.

### Keywords

Igfbp-3; cardioprotection; cardiotoxicity; cardiomyocytes; iPSC-CM; NRVM; transcriptomics; anthracycline; doxorubicin

## INTRODUCTION

Anthracyclines such as doxorubicin (Dox) are effective chemotherapeutic agents (1). Their use however is hindered by the risk of anthracycline-induced cardiotoxicity (AIC) (2). Despite recent advances in targeted therapies, ~33% of breast cancers and ~66% of lymphomas are treated with anthracyclines, while 50–60% of childhood cancer survivors have a history of anthracycline exposure (3). Whereas multiple injury pathways are implicated in AIC (1, 4, 5), a proposed unifying mechanism is the targeting of topoisomerase IIb (Top2β) which regulates topological changes during DNA transcription. Formation of a Top2β -Dox-DNA cleavage complex leads to DNA double-strand breaks (DSB), perturbation of transcription pertinent to cardiomyocyte (CM) energetics and function, phosphorylation of the DNA DSB response coordinator histone H2AX (γ-H2AX), and CM death (6). However, our understanding of CM injury response pathways at play following anthracycline treatment remains incomplete.

Whereas prior transcriptomic studies reported insulin-like growth factor (IGF) binding protein (IGFBP) 3 (Igfbp-3) induction by Dox (7, 8), its role in AIC remains ill-defined. Igfbp-3 is the most abundant IGFBP family member in the circulation (9), and can either inhibit the proliferative effect of IGFs by restricting their access to receptors or potentiate IGF actions by increasing the phosphorylation of IGF receptors (10). Igfbp-3 can act as a secreted circulating factor as well as an intracellular molecule implicated in major signaling pathways. Indeed, beyond their IGF-dependent actions, a direct and context-dependent role

for Igfbp-3 in DNA damage and apoptosis has been suggested. In cancer cells, whereas Igfbp-3 may potentiate DNA-damage induced apoptosis (11, 12), it also has a pro-survival effect through activation of sphingosine kinase-1, formation of nuclear complexes with epidermal growth factor receptor (EGFR) (13, 14), or suppression of oxidative stress (15). Immortalized H9C2 rat cardiomyoblast cells were previously used to study a pro-apoptotic effect of Igfbp-3 under concomitant serum starvation and Dox treatment (16), however these cells are known to have limited generalizability to primary cardiomyocytes (17).

In this setting, we investigated the molecular mechanisms as well as systems-level transcriptomic effects of manipulating Igfbp-3 abundance in AIC using neonatal rat ventricular myocytes (NRVM), whose identical genetic background facilitates causality studies, and human induced pluripotent stem cell-derived cardiomyocytes (iPSC-CM), which permit a patient-specific approach for precision medicine. Our results indicate that these two model systems provide complementary information in AIC, and that Igfbp-3 has a protective effect in AIC by reducing DNA DSB, impeding Top2β expression, and alleviating detyrosinated microtubule accumulation, which reduces cardiomyocyte stiffness and improves contractile function (18).

## MATERIALS AND METHODS

### NRVM isolation and culture

Culture plates were coated with 0.1% gelatin before use. NRVM were prepared as previously described (19), and maintained in DMEM supplemented with 10% fetal bovine serum (FBS) for 24h. The medium was then replaced with fresh DMEM supplemented with 1% Insulin-Transferrin-Selenium (ITS-G, ThermoFisher, Waltham, MA, USA), before transfection or drug treatment.

### iPSC-CM differentiation and culture

iPSC-CM were differentiated from a human iPSC cell line (iPS23 UCLA, Los Angeles, CA, USA) using a previously described method (20, 21). Briefly, iPSCs were maintained in mTeSR1 (Stemcell Technology, Vancouver, Canada). Culture plates were coated with 0.1% gelatin before use. RPMI1640 supplemented with B27 minus insulin (Invitrogen, Waltham, MA, USA) was used as differentiation medium. On day 0–1, 6 μM CHIR99021 (Selleckchem, Houston, TX, USA) was added to the differentiation medium. Between day 3–5, 5 μM IWR1 (Sigma-Aldrich, St. Louis, MO, USA) was added to refresh the differentiation medium. After day 7, the medium was replaced with RPMI1640 plus B27 maintenance medium. From day 10–11, RPMI 1640 without D-glucose, supplemented with B27, was transiently used for metabolic purification of cardiomyocytes. Purity of iPSC-CM was assessed by cardiac troponin T positivity (Abcam, Cambridge, UK) on confocal imaging and confirmatory expression of cardiomyocyte markers including NK2 homeobox-5, myosin heavy chain (MYH)-6, MYH-7, and myosin light chain-7 by PCR.

### Adenoviral transduction, siRNA silencing, and doxorubicin treatment

The structure of adenoviruses used is depicted in Fig. S3E–H. NRVM were transduced with adenovirus expressing rat Igfbp-3 (Vector Biolabs, San Francisco, CA, USA), rat n-terminus

3xFLAG Igfbp-3 (Abmgood, Richmond, BC, Canada), and negative control adenovirus (Ad-Null, Vector Biolabs) with a multiplicity of infection (MOI) of 10. Negative control siRNA, rat Igfbp-3 siRNA (Qiagen, Hilden, Germany) were transfected into NRVM using lipofectamine RNAiMAX (Thermo Fisher) according to the manufacturer's instruction. iPSC-CM were transduced with adenovirus expressing human Igfbp-3 and human Igfbp-3 shRNA (Vector Biolabs) with a MOI of 30. 48h after transduction or transfection, NRVM and iPSC-CM were treated with 1μM Dox (Sigma-Aldrich) for 24h (7). qPCR primers used to verify the overexpression and knockdown are:

Human Forward Primer: AGAGCACAGATACCCAGAACT

Human Reverser Primer: GGTGATTCAGTGTGTCTTCCATT

Mouse Forward Primer: CCAGGAAACATCAGTGAGTCC

Mouse Reverser Primer: GGATGGAACTTGGAATCGGTCA

Rat Forward Primer: TTCCTCAATGTGCTGAGTCCC

Rat Reverser Primer: TTTCCCCTTGGTGTCATAGCC

### Dox injection in neonatal and adult mice

C57Bl/6 mice (Jackson Labs, Bar Harbor, ME, USA) were used for all injections. For neonatal mice, 10 mg/kg Dox was injected IP into the lower left abdominal quadrant at P1, and the hearts harvested at P2. For adult mice, 20 mg/kg Dox was injected IV through the tail-vein and the hearts harvested 24h after injection. Phosphate-buffered saline (PBS) was injected in control animals. All animals are randomly allocated for treatments.

### Immunofluorescent staining and confocal imaging

NRVM, iPSC-CM and OCT embedded heart sections were fixed with 4% paraformaldehyde for 15 min, and permeabilized with 0.25% Triton X-100 (Sigma-Aldrich) in PBS for 20 min. at room temperature (RT). Samples were then incubated with 2% BSA in PBS at RT for 30 min. to block non-specific binding, and incubated with 1 μg/mL primary antibody in 2% BSA diluted in PBS with gentle shake for 1h at RT. Samples were washed in PBS for 5 min. three times, incubated with secondary antibody in 2% BSA for 1h at RT in the dark and washed in PBS for 5 min. three times. DAPI was used for nuclear counter staining and cells were imaged with a Leica TCS SP8 confocal microscope. For STED imaging, Alexa 594 and Atto 647N were used for dual channel imaging and fluorophore deactivation were achieved by a 775nm laser. The theoretical resolution was adjusted to about 30nm lateral and 80nm axial. The area of tubulin and detyrosinated tubulin was analyzed with ImageJ by quantifying pixels with an intensity higher than 15 (256 maximum) to exclude background noise.

### Western blotting

Proteins were extracted from cells or hearts with M-PER Mammalian Protein Extraction Reagent supplied with Halt Protease Inhibitor Cocktail (ThermoFisher). Lysates were

centrifuged at 18000g to remove cellular debris and protein concentration was determined by Pierce Rapid Gold BCA Protein Assay Kit (ThermoFisher). 20 μg protein was loaded for each experimental condition and the membrane was stained with 1 μg/mL primary antibody in 2% BSA overnight, followed by secondary antibody for 2h at RT.

### Cell fractionation assay

NRVM were washed twice with PBS and dissociated with TrypLE Express Enzyme (ThermoFisher). Cell fractionation was performed using the Abcam Cell Fractionation Kit according to the manufacturer's protocol. Briefly, cells were re-suspended to $6.6 \times 10^6$ cells/mL, and cytoplasmic fraction and membrane fraction were extracted with Detergent I and Detergent II diluted with Buffer A.

### Phase-contrast imaging and contraction assays for iPSC-CM

Phase-contrast images were captured using a Zeiss LSM880 spinning disk confocal microscope in a humidified chamber at 37 °C and 5% $CO_2$. Contraction data were extracted using Pulse Contractility Assay (22).

### RNA sequencing of NRVM and iPSC-CM and data analysis

Total RNA was extracted using Rneasy Mini Kits (Qiagen). Nanodrop (ThermoFisher) and Agilent TapeStation were used for quality control of RNA integrity. Ribosomal RNA depletion was performed using Ribo-Zero Plus rRNA Depletion Kit (Illumina, San Siego, CA, USA). cDNA synthesis, library preparation and sequencing on a Novaseq S4 instrument (Illumina) was performed (UCLA Technology Center for Genomics & Bioinformatics). 2×150 bp sequencing strategy was adopted and an average of 55.5 million reads for each sample acquired. Raw reads were aligned to the rat (mRatBN7.2) or human (grch38) transcriptome by Salmon using default parameters (23), and only genes that had a minimum of 20 reads in all samples combined were analyzed. DEGs were identified with DESeq2 (24) and an adjusted P-value (Padj) <0.05 was used as the cutoff threshold for statistical significance between biological conditions. For GSEA, normalized counts from DESeq2 were used as input and FDR <0.25 was used as the cutoff threshold (25).

### Integration of single-cell cardiomyocyte transcriptomics with NRVM and iPSC-CM datasets

Single cell RNA-Seq data of P0 to P28 mouse cardiomyocytes was obtained from GEO Accession GSE165917 (26). iPSC-CM and NRVM were sequenced by bulk RNA-seq and sample names replaced with artificial barcodes in the data matrix to permit integration with mouse CM single-cell data by adopting a previously described method (27). The datasets were first normalized by the total counts of each sample or cell followed by a log normalization. Cells were then filtered based on genes detected (greater than 3000 genes per cell), and the top 2000 highly variable genes were used as 'anchors' for integration. Standard single-cell data analysis was then performed with Seurat4.0 (28). Significant principal components (PCs) were determined using the JackStraw procedure and the top 9 PCs were used to generate UMAPs (uniform manifold approximation and projection) and cell clusters. The pseudo-time trajectory analysis was performed using Monocle3 default workflow (29).

### WGCNA network construction

WGCNA was performed to construct co-expression networks for NRVM and iPSC-CM (30). Briefly, unsigned network was chosen for all analyses to include negative correlations. Pearson correlation was used for network construction and soft-thresholding was adjusted for the scale-free topology before calculating the adjacency matrix. The size of the modules was established by using a mergeCutHeight parameter of 0.2 in the blockwiseModules function.

### Cancer cell proliferation

Cancer cell lines were obtained from the American Type Culture Collection (ATCC, Manassas, VA, USA), seeded at 10'000 cells/well in a 96-well plate, treated with Dox (0.2, 1, and 5 μM), with and without dexrazoxane (200 μM) for 24h. Cancer cells were also transduced with Ad Null (control), Ad Igfbp-3, and Ad Igfbp-3 shRNA for 48h with a MOI (multiplicity of infection) of 30, followed by Dox and/or dexrazoxane for 24h. Cancer cell metabolic activity was determined by a luminescence-based 'MTT' ((3-[4,5-dimethylthiazol-2-yl]-2,5-diphenyltetrazolium bromide) assay requiring NAD(P)H-dependent oxidoreductase enzymatic activity for the formation of formazan (Abcam) (31). We also measured total cancer cell protein content with sulforhodamine B (SRB) (Abcam) (32). Cancer cells were fixed and the amount of protein-bound SRB measured fluorometrically (Ex/Em = 488/585 nm) (33).

### Statistics

For all remaining statistical analyses, Student's t test (two-sided) was used to compare the differences between two data-sets. For comparisons among multiple groups, one-way ANOVA was used and Dunnett's test was used to correct for multiple comparisons and calculate adjusted P-values. A P-value $< 0.05$ was considered statistically significant (*$P < 0.05$; **$P < 0.01$; ***$P < 0.001$). Unless stated otherwise, all data in bar graphs are presented as mean ± standard deviation.

### Study approval

All animal studies were approved by the Animal Research Committee of the University of California, Los Angeles.

## RESULTS

### Igfbp-3 is significantly induced by Dox in NRVM, and in neonatal and adult mouse hearts

We first determined Igfbp-3 expression changes *in vitro* and *in vivo* following Dox (Fig. S1). Treating NRVM with Dox led to a 3.4 and 4.2-fold increase in Igfbp-3 mRNA level after 6 and 12h, respectively ($n=3$, $P<0.05$), followed by normalization to control levels at 24h (Fig. S1A). Immunoblotting of the same cells demonstrated a time-dependent increase in Igfbp-3 protein expression following Dox (Fig. S1D). Dox injection in postnatal day 1 (P1) mice led to a 6.6-fold induction of Igfbp-3 mRNA ($n=5$, $P<0.01$) and an increase in protein level in P2 hearts (Fig. S1B,E). Similarly, Dox treated adult mice significantly upregulated cardiac Igfbp-3 at 24h, demonstrated by mRNA and immunofluorescent staining (IF) (Fig. S1C,F).

Examination of the Igfbp-3 sequence homology in human, mouse, and rat by Clustal Omega (34) indicates an 89% degree of similarity between these species (Fig. S2). Taken together, these results indicate that Igfbp-3 is similarly and robustly induced by different species in cardiomyocytes following Dox treatment.

### Dox induces Igfbp-3 nuclear translocation

To determine the cellular compartments in which Igfbp-3 is localized under physiological and Dox conditions, we overexpressed Igfbp-3 with N-terminus 3xFLAG tag in NRVM (Fig. S3). Immunofluorescence (IF) and cell fractionation demonstrated that under physiological conditions, Igfbp-3 is expressed uniformly in the cytoplasm, membrane, and nucleus. However, Dox diminishes cytoplasmic Igfbp-3 leading to a relative enrichment of the nuclear component (Fig. 1A,B). IF of empty vector indicates specificity of the 3xFLAG overexpression (Fig. S4). Endogenous Igfbp-3 has a similar nuclear enrichment pattern following Dox (Fig. S5).

### Igfbp-3 attenuates Dox-induced DNA damage in CM

To assess whether Igfbp-3 affects Top2β-Dox-DNA cleavage complex-induced DNA DSB, we modulated Igfbp-3 levels in NRVM under Dox. The overexpression and knockdown of Igfbp-3 in NRVM are shown (Fig. S3A,B,F). Igfbp-3 overexpression led to a 56% reduction of γ-H2AX protein levels after Dox at 12h ($n=3$, $P<0.05$) (Fig. 1C), while Igfbp-3 silencing potentiated the phosphorylation of H2AX at 12 and 24h (Fig. 1D). We further observed that Igfbp-3 overexpression in Dox-treated NRVM led to a 44% reduction of Top2β protein levels ($n=3$, $P<0.01$) (Fig. 1E). However, we did not observe a change in cell death by TUNEL assay and LDH release assay when modulating Igfbp-3 in NRVM (Fig. S6). These results suggest that manipulating Igfbp-3 alone is not sufficient to rescue Dox-induced cardiomyocyte death.

### Igfbp-3 manipulation has no effect on the chemotherapeutic effect of Dox in cancer cells

We further determined whether Igfbp-3 interferes with the chemotherapeutic effect of Dox in cancer cells and compared results with dexrazoxane, used clinically to mitigate AIC (Fig. S7). There was no significant effect of Igfbp-3 expression modulation in the MDA-MB-231 line of highly aggressive, invasive, and poorly differentiated triple-negative human adenocarcinoma breast cancer lacking estrogen receptor and progesterone receptor expression, as well as human epidermal growth factor receptor-2 (HER-2) amplification (Fig. S7A, B) (35), nor in the T47D line of human breast ductal carcinoma cells expressing progesterone receptors (Fig. S7C, D) (36). At very low Dox dose (0.2 μM), Igbfp-3 was associated with a mild increase in triple-negative breast cancer cell metabolic activity, however this was not observed at higher doses of Dox, nor was there a difference in cancer cell protein content when perturbing Igfbp-3 expression.

### Distinct transcriptomic profiles of NRVM and iPSC-CM

To better dissect the molecular mechanisms by which Igfbp-3 mitigates AIC, we performed RNA sequencing in both NRVM and iPSC-CM following Igfbp-3 modulation under physiologic or Dox conditions. We first aimed to compare the variations in NRVM and

iPSC-CM transcriptomic profiles under Dox alone, i.e. without Igfbp-3 manipulation (Fig. S8). Dox treatment led to n=2195 upregulated differentially expressed genes (DEGs) and n=2671 downregulated DEGs in NRVM (Fig. S8A, Table S1), and n=4938 upregulated DEGs and n=4270 downregulated DEGs in iPSC-CM (Fig. S8B, Table S2). Among these, n=1179 were common upregulated DEGs and n=1110 common downregulated DEGs to the two cell systems (Fig. S8C). Gene ontology (GO) analyses revealed that common upregulated DEGs are enriched in cell death pathways and genotoxicity, and common downregulated DEGs in muscle development and cardiac contraction (Fig. S8D–E). Comparing NRVM and iPSC-CM transcriptomics under physiological condition reveals that NRVM express higher levels of carbohydrate metabolism and mitotic cell cycle genes, while iPSC-CM is enriched in cell junction organization and muscle development genes (Fig. S8F–G). Interestingly, both carbohydrate metabolism and cell cycle gene expression are major characteristics of immature CM (37), suggesting a less mature state of NRVM compared to iPSC-CM.

To further scrutinize the maturation stage of NRVM and iPSC-CM, we adopted an open-source method permitting the comprehensive integration of transcriptomic datasets using the top differentially expressed genes to determine identity ‘anchors’ (27). We assigned artificial barcodes to each NRVM and iPSC-CM RNA-seq control sample and integrated these with a publicly available reference single cell transcriptomic dataset that characterized the maturation of purified mouse CM from P0 to P28 (26). Cell clustering (Fig. S8H) demonstrated that mouse CM clustered well based on their age, NRVM clustered with P0 CM, and iPSC-CM was close to P14 CM. Pseudotime analysis corroborated that NRVM and P0 CM are the earliest in maturation or pseudotime stage, while iPSC-CM exhibit a maturation stage between P7 and P14 CM (Fig. S8I). Interestingly, compared with more mature CM (iPSC-CM, P14, P21, P28) that express well-established CM markers such as *Tcap, Ckmt2, Mb,* and *Ankrd1*, less mature CM (NRVM, P0, P7) express higher levels of fibroblast marker genes such as *Fabp4, Col1a1, Vim, Col1a2, Col3a1* and *Postn* (Fig. S8J,K). Overall, these data demonstrate that NRVM and iPSC-CM have distinct transcriptomic profiles, and that iPSC-CM exhibit a more mature CM expression repertoire compared to NRVM, setting the stage for our subsequent analyses perturbing Igfbp-3 expression under Dox treatment in both cardiomyocyte types.

## NRVM and iPSC-CM provide complementary information to dissect the protective role of Igfbp-3 in AIC

- **Igfbp-3 modulation under physiological conditions—**The overexpression and knockdown of Igfbp-3 in iPSC-CM are shown (Fig. S3C,D,G,H). Overexpression of Igfbp-3 led to n=159 upregulated DEGs and n=410 downregulated DEGs in iPSC-CM under physiological condition (Fig. 2A, Table S3). *Megf10* ($Log_2FC=2.5$, Padj=0.0007), which plays an important role in muscle cell proliferation and motility (38), and *Sgpp2* ($Log_2FC=1.2$, Padj=$2\times10^{-8}$), which degrades sphingosine 1-phosphate, associated with heart failure (39), were among the most significant upregulated DEGs. Well-established heart failure biomarkers, *Nppa* ($Log_2FC=-1.78$, Padj=$1\times10^{-57}$) *and Nppb* ($Log_2FC=-2.73$, Padj=$1\times10^{-62}$) (40), were among the most significant downregulated DEGs with Igfbp-3 overexpression.

Silencing of Igfbp-3 under physiological conditions in iPSC-CM led to n=312 upregulated DEGs and n=460 downregulated DEGs (Fig. 2B, Table S4). Genes that regulate cytoskeleton structure such as *Actb, Map2 and Celf1* were significantly upregulated, while downregulated DEGs involve oxidative phosphorylation genes such as *Pdk4, Ndufb5 and Gpi*, as well as glycolysis genes such as *Aldoa, Aldoc, Acly, Pkm and Tpi1*, suggesting an important role of Igfbp-3 in the metabolic activity of iPSC-CM under physiological condition.

- **Igfbp-3 perturbation following Dox treatment—**Following Dox, Igfbp-3 overexpression led to n=8 significant upregulated DEGs and n=23 downregulated DEGs (Fig. 2C, Table S5). *Slc16a6* ($Log_2FC=0.93$, Padj=0.003), a small molecule transporter that catalyzes the transport of pyruvate and branched-chain amino acids (41), and *Cpt1b* ($Log_2FC=1.5$, Padj=0.03), a rate-controlling enzyme of the long-chain fatty acid beta-oxidation in muscle mitochondria (42), were among the most significantly upregulated DEGs. Interestingly, *Nppa* ($Log_2FC=-1.12$, Padj=0.0001) *and Nppb* ($Log_2FC=-1.69$, Padj=0.04) were significantly downregulated by Igfbp-3 under Dox conditions, similar to the above results under physiologic conditions. Silencing of Igfbp-3 in iPSC-CM under Dox led to n=13 upregulated DEGs and n=8 downregulated DEGs (Fig. 2D, Table S6). The most significantly regulated DEGs were *Actb, Tuba1c, Serpinb4, Serpinb7, Syndig1,* and *Wdr47*.

Transcriptional expression of the heart failure markers *Nppa* and *Nppb* were consistantly downregulated by Igfbp-3 overexpression under both control and Dox treatment. We evaluated the RNA-seq data by assessing Western blotting of protein expression (Fig. S9). *Nppa* levels decreased (borderline not significant with a P=0.06) when overexpressing Igfbp-3 under control conditions, whereas *Nppb* decreased significantly. This was not the case however under Dox conditions at the 24h mark. Contrary to results with mRNA, no changes in *Map2* protein levels were observed when overexpressing and silencing Igfbp-3.

Compared to the iPSC-CM (Fig. 2A–D), fewer genes were differentially regulated by Igfbp-3 modulation in NRVM (Fig. 2E). In control NRVM, Igfbp-3 overexpression led to a significant downregulation of *Yif1b*, and a significant upregulation of *Pigg*. Silencing Igfbp-3 led a significant downregulation of *Ralb,* required for CM autophagy (43). Under Dox, Igfbp-3 overexpression led to a significant downregulation of *Aldh18a1, Med22* and *Retreg1*, implicated in endoplasmic reticulum autophagy (44), and a significant upregulation of *Pigg* and *Armcx1*, associated with neuronal survival and axonal regeneration (45). Silencing Igfbp-3 led to a significant upregulation of *Zfp622*, which positively regulates apoptosis signal-regulating kinase-1 (*Ask1*) (46), and *Snip1*, which increases c-Myc activity and inhibits TGF-b and NF-kB signaling (47).

The overlapping differentially regulated genes between conditions are summarized in Fig. S10.

## Gene pathways affected by Igfbp-3

To better dissect genome-wide RNA expression patterns in AIC perturbed by Igfbp-3 modulation, we conducted gene set enrichment analyses (GSEA) to characterize the biological pathways involved. When overexpressing Igfbp-3 under Dox in iPSC-CM, enriched pathways included oxidative phosphorylation (normalized enrichment score

[NES=1.27, false-discovery rate [FDR]=0.176) and fatty acid metabolism (NES=1.34, FDR=0.176) (Fig. 3A). *Idh3g*, which encodes one of the rate-limiting enzymes in the tricarboxylic acid cycle (48), *Ndufv1*, which regulates mitochondrial complex I activity (49) and *Cel*, a lipolytic enzyme that regulates lipid and fatty acid metabolism (50), were among the core enrichment genes in these pathways. In accordance with the reduction of γ-H2AX level in NRVM when overexpressing Igfbp-3 (Fig. 1C–D), GSEA further revealed a negative enrichment of the apoptosis pathway, driven by genes such as *Anxa1, Casp4* and *Casp2* in iPSC-CM (NES=−2.14, FDR=0.003). Overall, these data indicate that overexpression of Igfbp-3 is associated with an enrichment in pathways associated with CM metabolic activity and a diminution in the apoptosis pathway which is activated in iPSC-CM treated with Dox.

Reciprocally, when silencing Igfbp-3 in iPSC-CM under Dox, we observed a positive enrichment in the apoptosis pathway (NES=1.56, FDR=0.016) (Fig. 3B), driven by genes such as *Tnfrsf12a, Anxa1,* and *Rhob*. Similarly, TNF-a signaling via NF-kB was another positively enriched pathway (NES=2.19, FDR=0.001). In contrast with the positive enrichment of metabolic activity genes when overexpressing Igfbp-3, key branched-chain amino acid (BCAA) catabolism genes such as *Bcat1, Bckdhb* and *Bckdha*, were negatively enriched when silencing Igfbp-3 (NES=−2.03, FDR=0.028). Combined, these findings underscore that silencing of Igfbp-3 in iPSC-CM under Dox leads to an enrichment in pathways implicated in apoptosis and CM dysfunction.

## Igfbp-3 networks and modules

We further conducted network analysis and module construction by adopting Weighted Gene Correlation Network Analysis (WGCNA) (30) of genes co-expressed with Igfbp-3 for both iPSC-CM (Fig. 3C) and NRVM (Fig. 3D) under Dox. We observed that microtubule related genes such as *Tub-a1a, -a1c, -b2a, -b6,* and *Des* are in the same co-expression network as Igfbp-3, and *Tub-a1a* and *-a1c*, whose expression levels negatively correlate with Igfbp-3, are among the top 5 hub genes with n=49 and n=48 connections, respectively, in the network (average gene connectivity = 20, range = 3–49) (Fig. 3C). *Limk1* (n=47 connections) was identified as another top 5 hub gene in the iPSC-CM network, and there is a negative correlation between *Limk1* and Igfbp-3 expression. *Limk1* is associated with actin polymerization, and inhibition of *Limk1* improves ventricular remodeling and alleviates cardiac dysfunction (51). Within the same network, we note additional cytoskeleton proteins such as *Tnni3, Nes, Cytor, Txnrd1,* and *Acta1*, further supporting an association of Igfbp-3 function with the CM cytoskeleton. Genes involved in heart failure such as *Ace2, Nppa,* and *Ankrd2* have a negative correlation with Igfbp-3 and are co-expressed in the same network.

For the NRVM network under Dox (Fig. 3D), *Bgn*, required for adaptive remodeling after myocardial infarction, positively correlates with Igfbp-3 (52), and is significantly downregulated when silencing Igfbp-3 in iPSC-CM. Interestingly, *Vash1*, another mediator of CM microtubule stiffness, is present in the Igfbp-3 NRVM network. *Vash1* negatively correlates with Igfbp-3 and is significantly downregulated by Igfbp-3 overexpression in iPSC-CM. Downregulation of *Vash1* can lower the stiffness of microtubules and promote cardiac contraction and relaxation in failing human CM (53). Therefore, the negative correlation of *Vash1* with Igfbp-3 further supports our observations that Igfbp-3

assoicates with genes implicated in CM contraction by alleviating microtubule dysfunction, providing complementary results with the iPSC-CM network. Igfbp-3 networks under control condition in iPSC-CM and NRVM are illustrated in Fig. S11.

## Igfbp-3 alleviates detyrosinated microtubule accumulation

Tubulin family genes are the most consistently regulated by Igfbp-3 in the iPSC-CM transcriptomic dataset. Under control condition, overexpression of Igfbp-3 leads to a significant downregulation of *Tub-a1b, -a1c, -b2a, -b3, -b4b, -b6, and Des* (Fig. 2A). Under Dox, overexpression of Igfbp-3 similarly leads to a significant downregulation of *Tub-a1c, -b2a, Des, and Txnrd1* (Fig. 2C). GSEA further indicates a negative enrichment (downregulation) of actin and tubulin folding genes (NES=−1.21, FDR=0.123, Fig. 3A). Reciprocally, Igfbp-3 silencing leads to a significant induction of *Tuba1c* and a significant downregulation of *Wdr47*, which stabilizes microtubules (54) (Fig. 2D). There is also a positive enrichment (upregulation) in GSEA of actin and tubulin folding genes when silencing Igfbp-3 (NES=2.01, FDR=0.003, Fig. 3B). Combined, these findings suggest that Igfbp-3 expression is associated with less tubulin accumulation and folding.

To further corrobate the transcriptomic results, we performed Stimulated Emission Depletion (STED) microscopy to assess tubulin accumulation in iPSC-CM with Igfbp-3 overexpression or silencing after Dox treatment. We observed a 21% increase measured by pixel area in detyrosinated tubulin normalized to total α-tubulin in iPSC-CM when silencing Igfbp-3 ($P<0.05$) (Fig. 4A,B). Quantitative Western blotting demonstrated a 62% increase in detyrosinated tubulin when silencing Igfbp3 in iPSC-CM compared with cells treated with control vector ($P<0.05$), and a 189% increase compared with cells overexpressing Igfbp3 ($P<0.0001$) (Fig. 4C). Additionally, quantitative Western blotting further demonstrated a 44% reduction in detyrosinated tubulin by Igfbp-3 overexpressing cardiomyocytes.

## Igfbp-3 knockdown leads to reduced contractile function in iPSC-CM after Dox treatment

Detyrosinated microtubules accumulate in failing human hearts, stiffening cardiomyocytes and impeding contractile function (55). To investigate whether Igfbp-3 affects CM contractility, we perturbed Igfbp-3 expression in iPSC-CM under physiological and Dox conditions. Under physiological condition, neither overexpression nor silencing of Igfbp-3 altered iPSC-CM contractility; however, Igfbp-3 silencing significantly decreased iPSC-CM contraction rate by 26% (38 beats per minute [BPM] to 28 BPM) compared with control ($P<0.001$) and by 19% (34 BPM to 28 BPM) compared with Igfbp-3 overexpression group ($P<0.05$) (Fig. S12). Under Dox treatment, Igfbp-3 silencing led to a significant decrease in contraction magnitude from 2.2 to 1.5 pixels (32%, $P<0.01$) compared with control, and from 2.0 to 1.5 pixels (25%, $P<0.05$) compared with Igfbp-3 overexpression (Fig 4D,E). When quantifying contraction velocity, there was a significant decrease from 13.1 to 10.1 pixel/sec (23%, $P<0.05$) compared with control, and a similar significant decrease from 13.5 to 10.1 pixels (25%, $P<0.01$) compared with Igfbp-3 overexpression (Fig. 4F,G), suggesting an important role of Igfbp-3 in maintaining cardiomyocyte contractility in the setting of Dox-induced cardiotoxicity (Video S1–3).

### Protective mechanisms implicating Igfbp-3 in the setting of AIC

We present a schematic diagram summarizing our experimental findings (Fig. 5). Igfbp-3 is significantly induced by Dox in CM. Following Dox treatment, Igfbp-3 expression diminishes in the cytoplasm and is enriched in the nuclear compartment. Igfbp-3 overexpression in cardiomyocytes impedes Top2β expression and reduces Top2β -Dox-DNA cleavage complex-induced DNA DSB, demonstrated by decreased γ-H2AX levels. In parallel, Igfbp-3 overexpression is associated with downregulation of the heart failure markers *Nppa* and *Nppb*, and further leads to a significant upregulation of *Cpt1b, Idh3g,* and *Ndufv1* which positively regulate cellular metabolic activity. Additionally, silencing Igfbp-3 attenuates contractile function in iPSC-CM after Dox treatment in the context of upregulation of tubulin family genes and detyrosinated microtubule accumulation, while overexpressing Igbfp-3 leads to downregulation of tubulin family genes.

## DISCUSSION

Anthracycline compounds may induce off-target cardiac injury. Whereas multiple pathobiological mechanisms are at play, and no single pathway can fully recapitulate all aspects of AIC, formation of a Top2β-Dox-DNA cleavage complex has been proposed as a key mediator of DNA DSB, transcriptional perturbation, and CM death, complicated by cardiac fibrosis and heart failure (56–58). Biological processes and protective mechanisms operating within CM to offset anthracycline-induced injury remain ill-defined (59).

Whereas previously associated with an antiproliferative effect in cancer cells (60–62), recent studies in triple negative breast cancer cells indicate Igfbp-3 has an obligatory role in the DNA repair response by activating EGFR and DNA-dependent protein kinase (DNA-PKcs) mediated nonhomologous end-joining (NHEJ) (63), as well as poly(ADP-ribose) polymerase-1 (PARP1) mediated DNA repair (64). Whereas an adverse effect of Igfbp-3 overexpression was observed on Dox chemotherapeutic efficacy at very low (subtherapeutic) doses of Dox in undifferentiated breast cancer cells, this was not the case at higher (therapeutic) doses of Dox, nor in differentiated breast cancer cells. Indeed, when taking into account the pharmacokinetic profile of Dox in humans, a single dose of 60 mg/m$^2$ typically results in a peak plasma concentration of 2–6μg/mL, with an average value of 6.9μM (65). Whether Igfbp-3 perturbation impedes Dox treatment efficacy will require further investigation using pertinent *in vivo* disease models.

Given its robust induction in CM by Dox and its context-dependent effect in apoptosis and DNA repair, we aimed to dissect the role of Igfbp-3 in AIC, not addressed previously. Our findings indicate that Igfbp-3 alleviates Dox-mediated phosphorylation of histone H2AX – an early and sensitive marker of DNA DSB – and downregulates Top2β expression whose CM-specific deletion protects mice from the development of AIC (6), both of which suggest a protective effect of Igfbp-3 against Dox-induced toxicity in CM. Whereas no direct effect of Igfbp-3 modulation on cardiomyocyte cell death was observed *in vitro*, additional studies are warranted to evaluate this *in vivo*, particularly under the spatial and temporal control of Igfbp-3 gene editing in relation to anthracycline exposure.

Our results further demonstrate that CM overexpression of Igfbp-3 protects against Dox-induced injury, as illustrated by the diminution of apoptotic genes *Anxa1, Casp2, Casp4,* and *Zfp622*, actin and tubulin folding genes, and the heart failure markers *Nppa* and *Nppb*, and the enrichment of genes positively regulating metabolic activities such as *Cpt1b, Idh3g* and *Ndufv1*. Concomitantly, gene set enrichment analyses reveal a positive enrichment of genes involved in oxidative phosphorylation and fatty acid metabolism and reciprocally a negative enrichment of genes involved in apoptosis. On the other hand, silencing of Igfbp-3 under Dox treatment leads to the positive enrichment of pro-apoptotic genes such as *Tnfrsf12a, Anxa1,* and *Rhob*, and TNF-a signaling via the NF-kB pathway, whose activation is also associated with CM apoptosis (66), and to the negative enrichment of actin and tubulin folding and BCAA catabolism, whose defect is a metabolic hallmark of the failing heart (67). The correlation between RNA-seq and protein expression is generally considered to be moderate, with reported correlation coefficients ranging from appr. 0.5–0.8 (68, 69). Therefore, there is an expected level of discrepancy between RNA-seq results and actual protein expression. Our observations with transcriptomic networks will thus require further validation, for example in proteomic networks and in pertinent *in vivo* experimental models of Igfbp-3 expression modulation under physiologic and Dox injury conditions.

Doxorubicin causes microtubule network distortion (70) and affects tubulin post-translational modification (PTM) in cardiomyocytes (71). In both animal models and humans, microtubule PTM in CM, such as detyrosination, is associated with contractile dysfunction and heart failure (18, 72). During contraction, microtubules must accommodate the changing geometry of the myocyte by deforming into a sinusoidal buckled configuration together with the sacromere, and the interaction strength between microtubules and the sarcomere is highly dependent on the detyrosination state of the microtubules (55). When detyrosination is suppressed, microtubules can accommodate the contraction by sliding rather than buckling with the sarcomere, which decreases the overall stiffness of the myocyte and improves contraction. Conversely, accumulation of detyrosinated microtubule stiffens cardiomyocytes and impedes contractile function. Furthermore, accumulation of detyrosinated microtubule is also associated with impaired relaxation in heart failure patients with perserved ejection fraction, and reducing detryosination speeds both contration and relaxation of failing human cardiomyocytes (53). To scrutinize more detailed and specific pathways when overexpressing and knocking down Igfbp-3 in iPSC-CM, we performed GSEA, revealing tubulin family genes were regulated by Igfbp-3 manipulation in most conditions (Fig. 2A–D, 3A–B). Gene co-expression analyses revealed that microtubule-related genes such as *Tub-a1a, -a1c, -b2a, -b6*, and *Des*, and cytoskeleton-related genes such as *Tnni3, Nes, Cytor, Txnrd1,* and *Acta1*, were in the same co-expression network as Igfbp-3, and further that *Tub-a1a* and *-a1c* – whose expression levels negatively correlate with Igfbp-3 – are the central hub genes of the network (Fig. 3E). Therefore, we hypothesize that CM induce Igfbp-3 following Dox treatment in an effort to alleviate CM dysfunction by regulating the microtubule network. Although total microtubule levels were similar in Igfbp-3 manipulation, silencing of Igfbp-3 under Dox treatment led to a significant accumulation of detyrosinated microtubules (Fig. 4A–C), and a significant reduction in contraction magnitude, velocity, and beat rate in iPSC-CM (Fig. 4D–G), while there was no change under physiological condition (Fig. S12). Whereas silencing of Igfbp-3 led to a

degradation of contractility measures under Dox, we postulate that Igfbp-3 overexpression did not further improve iPSC-CM contractility due to their derivation from healthy donors. Indeed, the dependency of donor (patient) susceptibility to AIC and *in vitro* measures of Dox-induced changes in iPSC-CM contractility was previously demonstrated (7). In the case of iPSC-CM derived from healthy donors, exposure to clinically relevant concentrations of Dox such as the one used in our study does not cause significant changes in cardiomyocyte contraction (7, 65). Further research is needed to assess protective pathways implicating Igfbp-3 in iPSC-CM derived from patients with clinical AIC.

Integrating single-cell RNA-seq data from different conditions, technologies, and species, is feasible (73) provided at least a subset of cells represent a shared biological state, i.e. are a similar cell type, as was the case in our integration of NRVM, iPSC-CM, and mouse CM transcriptomics. Compared with the plethora of data we derived from the iPSC-CM transcriptomics, there were fewer genes that were significantly regulated by Igfbp-3 manipulation in NRVM. We posit that these distinct responses are due to the significant maturation gap between the two cell systems (Fig. 3). We assessed general pathways enriched in NRVM and iPSC-CM by gene ontology, which further supports our findings that iPSC-CM are in a maturation pseudotime between P7 and P14 CM, whereas NRVM are in P0 pseudotime, with ensuing distinct transcriptomic profiles. Our results are corroborated by a recent single-cell study characterizing the maturation of iPSC-CM and P0-P84 CM (74) that also suggested an overlap between iPSC-CM and P11-P14 CM.

In conclusion, our delineation of the protective role of Igfbp-3 in AIC using two complementary model systems, NRVM and iPSC-CM, provides novel insights into pathways implicating Igfbp-3 in the CM injury response, DNA damage mitigation, detyrosinated tubulin accumulation, and contractile function changes. Whereas the present results do not imply using Igfbp-3 clinically as a cardioprotective molecule in AIC, they do build a foundation for additional molecular studies and *in vivo* manipulation of Igfbp-3 in transgenic animal models to further investigate protective mechanisms and phenotypic changes induced by this molecule.

## Supplementary Material

Refer to Web version on PubMed Central for supplementary material.

## Acknowledgments

Supported by NIH R56HL158569, VA Merit BX004558, UCLA Cardiovascular Discovery Fund/Lauren B. Leichtman and Arthur E. Levine Investigator Award, and NIH NCATS UCLA CTSI UL1TR001881. The authors thank Mackram Hassanieh for his assistance in conducting experiments. The graphical abstract was created with BioRender.com.

## Data Availability Statement

Original RNA-seq data generated in this study are openly available and have been deposited to Gene Expression Omnibus (GEO): GSE206803 (https://www.ncbi.nlm.nih.gov/geo/query/acccgi?acc=GSE206803), titled Integrative Transcriptomics and Cell Systems Analyses Reveal Protective Pathways Controlled by Igfbp-3 in Anthracycline-Induced

Cardiomyocyte Injury. Single cell RNA-Seq data of P0 to P28 mouse cardiomyocytes was obtained from GEO Accession GSE165917 (https://www.ncbi.nlm.nih.gov/geo/query/acc.cgi?acc=GSE165917) (26). The data that support the findings of this study are available in the article and supplementary material.

## REFERENCES


1. Songbo M, Lang H, Xinyong C, Bin X, Ping Z, and Liang S. Oxidative stress injury in doxorubicin-induced cardiotoxicity. Toxicology Letters. 2019;307:41–8. [PubMed: 30817977]
2. Ewer MS, and Ewer SM. Cardiotoxicity of anticancer treatments. Nature Reviews Cardiology. 2015;12(9):547–58. [PubMed: 25962976]
3. McGowan JV, Chung R, Maulik A, Piotrowska I, Walker JM, and Yellon DM. Anthracycline Chemotherapy and Cardiotoxicity. Cardiovascular Drugs and Therapy. 2017;31(1):63–75. [PubMed: 28185035]
4. Amgalan D, Garner TP, Pekson R, Jia XF, Yanamandala M, Paulino V, et al. A small-molecule allosteric inhibitor of BAX protects against doxorubicin-induced cardiomyopathy. Nature Cancer. 2020;1(3):315–28. [PubMed: 32776015]
5. Ichikawa Y, Ghanefar M, Bayeva M, Wu R, Khechaduri A, Naga Prasad SV, et al. Cardiotoxicity of doxorubicin is mediated through mitochondrial iron accumulation. The Journal of Clinical Investigation. 2014;124(2):617–30. [PubMed: 24382354]
6. Zhang S, Liu X, Bawa-Khalfe T, Lu L-S, Lyu YL, Liu LF, et al. Identification of the molecular basis of doxorubicin-induced cardiotoxicity. Nature Medicine. 2012;18(11):1639–42.
7. Burridge PW, Li YF, Matsa E, Wu H, Ong S-G, Sharma A, et al. Human induced pluripotent stem cell-derived cardiomyocytes recapitulate the predilection of breast cancer patients to doxorubicin-induced cardiotoxicity. Nature Medicine. 2016;22(5):547–56.
8. Cheng D, Cao N, Chen J, Yu X, and Shuai X. Multifunctional nanocarrier mediated co-delivery of doxorubicin and siRNA for synergistic enhancement of glioma apoptosis in rat. Biomaterials. 2012;33(4):1170–9. [PubMed: 22061491]
9. Baxter RC. Insulin-like growth factor binding protein-3 (IGFBP-3): Novel ligands mediate unexpected functions. Journal of Cell Communication and Signaling. 2013;7(3):179–89. [PubMed: 23700234]
10. Johnson MA, and Firth SM. IGFBP-3: A cell fate pivot in cancer and disease. Growth Hormone & IGF Research. 2014;24(5):164–73. [PubMed: 24953254]
11. Butt AJ, Firth SM, King MA, and Baxter RC. Insulin-like Growth Factor-binding Protein-3 Modulates Expression of Bax and Bcl-2 and Potentiates p53-independent Radiation-induced Apoptosis in Human Breast Cancer Cells. Journal of Biological Chemistry. 2000;275(50):39174–81. [PubMed: 10998426]
12. Yoshino K, Motoyama S, Koyota S, Shibuya K, Usami S, Maruyama K, et al. IGFBP3 and BAG1 enhance radiation-induced apoptosis in squamous esophageal cancer cells. Biochemical and Biophysical Research Communications. 2011;404(4):1070–5. [PubMed: 21195059]
13. Lin Z, Gise Av, Zhou P, Gu F, Ma Q, Jiang J, et al. Cardiac-Specific YAP Activation Improves Cardiac Function and Survival in an Experimental Murine MI Model. Circulation Research. 2014;115(3):354–63. [PubMed: 24833660]
14. Martin JL, Lin MZ, McGowan EM, and Baxter RC. Potentiation of growth factor signaling by insulin-like growth factor-binding protein-3 in breast epithelial cells requires sphingosine kinase activity. The Journal of Biological Chemistry. 2009;284(38):25542–52. [PubMed: 19633297]
15. Natsuizaka M, Kinugasa H, Kagawa S, Whelan KA, Naganuma S, Subramanian H, et al. IGFBP3 promotes esophageal cancer growth by suppressing oxidative stress in hypoxic tumor microenvironment. American Journal of Cancer Research. 2014;4(1):29. [PubMed: 24482736]
16. Granata R, De Petrini M, Trovato L, Ponti R, Pons N, Ghè C, et al. Insulin-like growth factor binding protein-3 mediates serum starvation- and doxorubicin-induced apoptosis in H9c2 cardiac cells. Journal of Endocrinological Investigation. 2003;26(12):1231–41. [PubMed: 15055478]

17. Watkins SJ, Borthwick GM, and Arthur HM. The H9C2 cell line and primary neonatal cardiomyocyte cells show similar hypertrophic responses in vitro. In Vitro Cellular & Developmental Biology - Animal. 2010;47(2):125–31. [PubMed: 21082279]
18. Chen CY, Caporizzo MA, Bedi K, Vite A, Bogush AI, Robison P, et al. Suppression of detyrosinated microtubules improves cardiomyocyte function in human heart failure. Nature Medicine. 2018;24(8):1225–33.
19. MacLellan WR, Xiao G, Abdellatif M, and Schneider MD. A novel Rb- and p300-binding protein inhibits transactivation by MyoD. Molecular and Cellular Biology. 2000;20(23):8903–15. [PubMed: 11073990]
20. Li S, Ma F, Yokota T, Garcia G Jr., Palermo A, Wang Y, et al. Metabolic reprogramming and epigenetic changes of vital organs in SARS-CoV-2-induced systemic toxicity. JCI Insight. 2021;6(2):e145027. [PubMed: 33284134]
21. Lian X, Hsiao C, Wilson G, Zhu K, Hazeltine LB, Azarin SM, et al. Robust cardiomyocyte differentiation from human pluripotent stem cells via temporal modulation of canonical Wnt signaling. Proceedings of the National Academy of Sciences of the United States of America. 2012;109(27):E1848–E57. [PubMed: 22645348]
22. Maddah M, Heidmann JD, Mandegar MA, Walker CD, Bolouki S, Conklin BR, et al. A non-invasive platform for functional characterization of stem-cell-derived cardiomyocytes with applications in cardiotoxicity testing. Stem Cell Reports. 2015;4(4):621–31. [PubMed: 25801505]
23. Patro R, Duggal G, Love MI, Irizarry RA, and Kingsford C. Salmon provides fast and bias-aware quantification of transcript expression. Nature Methods. 2017;14(4):417–9. [PubMed: 28263959]
24. Love MI, Huber W, and Anders S. Moderated estimation of fold change and dispersion for RNA-seq data with DESeq2. Genome Biology. 2014;15(12):550–. [PubMed: 25516281]
25. Subramanian A, Tamayo P, Mootha VK, Mukherjee S, Ebert BL, Gillette MA, et al. Gene set enrichment analysis: a knowledge-based approach for interpreting genome-wide expression profiles. Proceedings of the National Academy of Sciences of the United States of America. 2005;102(43):15545–50. [PubMed: 16199517]
26. Murphy SA, Miyamoto M, Kervadec A, Kannan S, Tampakakis E, Kambhampati S, et al. PGC1/PPAR drive cardiomyocyte maturation at single cell level via YAP1 and SF3B2. Nature Communications. 2021;12(1):1648–.
27. Stuart T, Butler A, Hoffman P, Hafemeister C, Papalexi E, Mauck WM, 3rd, et al. Comprehensive Integration of Single-Cell Data. Cell. 2019;177(7):1888–902.e21. [PubMed: 31178118]
28. Hao Y, Hao S, Andersen-Nissen E, Mauck WM 3rd, Zheng S, Butler A, et al. Integrated analysis of multimodal single-cell data. Cell. 2021;184(13):3573–87.e29. [PubMed: 34062119]
29. Qiu X, Mao Q, Tang Y, Wang L, Chawla R, Pliner HA, et al. Reversed graph embedding resolves complex single-cell trajectories. Nature Methods. 2017;14(10):979–82. [PubMed: 28825705]
30. Langfelder P, and Horvath S. WGCNA: an R package for weighted correlation network analysis. BMC Bioinformatics. 2008;9:559–. [PubMed: 19114008]
31. Park K, Lee GY, Park R-W, Kim I-S, Kim SY, and Byun Y. Combination Therapy of Heparin–Deoxycholic Acid Conjugate and Doxorubicin against Squamous Cell Carcinoma and B16F10 Melanoma. Pharmaceutical Research. 2007;25(2):268–76. [PubMed: 17619999]
32. Skehan P, Storeng R, Scudiero D, Monks A, McMahon J, Vistica D, et al. New Colorimetric Cytotoxicity Assay for Anticancer-Drug Screening. JNCI Journal of the National Cancer Institute. 1990;82(13):1107–12. [PubMed: 2359136]
33. Vichai V, and Kirtikara K. Sulforhodamine B colorimetric assay for cytotoxicity screening. Nature Protocols. 2006;1(3):1112–6. [PubMed: 17406391]
34. Sievers F, Wilm A, Dineen D, Gibson TJ, Karplus K, Li W, et al. Fast, scalable generation of high-quality protein multiple sequence alignments using Clustal Omega. Molecular Systems Biology. 2011;7:539–. [PubMed: 21988835]
35. Cailleau R, Olivé M, and Cruciger QVJ. Long-term human breast carcinoma cell lines of metastatic origin: Preliminary characterization. In Vitro. 1978;14(11):911–5. [PubMed: 730202]
36. Sartorius CA, Groshong SD, Miller LA, Powell RL, Tung L, Takimoto GS, et al. New T47D breast cancer cell lines for the independent study of progesterone B- and A-receptors: only

antiprogestin-occupied B-receptors are switched to transcriptional agonists by cAMP. Cancer Research. 1994;54(14):3868–77. [PubMed: 8033109]

37. Guo Y, and Pu WT. Cardiomyocyte Maturation: New Phase in Development. Circulation Research. 2020;126(8):1086–106. [PubMed: 32271675]
38. Logan CV, Lucke B, Pottinger C, Abdelhamed ZA, Parry DA, Szymanska K, et al. Mutations in MEGF10, a regulator of satellite cell myogenesis, cause early onset myopathy, areflexia, respiratory distress and dysphagia (EMARDD). Nature Genetics. 2011;43(12):1189–92. [PubMed: 22101682]
39. Perez Carrillo L, Sanchez Lazaro I, Martinez Dolz L, Portoles M, Rosello-Lleti E, and Tarazon E. Implication of sphingolipid metabolism gene dysregulation and cardiac sphingosine-1-phosphate accumulation in heart failure. European Heart Journal. 2021;42.
40. Goetze JP, Bruneau BG, Ramos HR, Ogawa T, de Bold MK, and de Bold AJ. Cardiac natriuretic peptides. Nature Reviews Cardiology. 2020;17(11):698–717. [PubMed: 32444692]
41. Higuchi K, Sugiyama K, Tomabechi R, Kishimoto H, and Inoue K. Mammalian monocarboxylate transporter 7 (MCT7/Slc16a6) is a novel facilitative taurine transporter. The Journal of Biological Chemistry. 2022;298(4):101800–. [PubMed: 35257743]
42. van der Leij FR, Cox KB, Jackson VN, Huijkman NCA, Bartelds B, Kuipers JRG, et al. Structural and Functional Genomics of the CPT1B Gene for Muscle-type Carnitine Palmitoyltransferase I in Mammals. Journal of Biological Chemistry. 2002;277(30):26994–7005. [PubMed: 12015320]
43. Rifki OF, Bodemann BO, Battiprolu PK, White MA, and Hill JA. RalGDS-dependent cardiomyocyte autophagy is required for load-induced ventricular hypertrophy. Journal of Molecular and Cellular Cardiology. 2013;59:128–38. [PubMed: 23473774]
44. Khaminets A, Heinrich T, Mari M, Grumati P, Huebner AK, Akutsu M, et al. Regulation of endoplasmic reticulum turnover by selective autophagy. Nature. 2015;522(7556):354–8. [PubMed: 26040720]
45. Cartoni R, Norsworthy MW, Bei F, Wang C, Li S, Zhang Y, et al. The Mammalian-Specific Protein Armcx1 Regulates Mitochondrial Transport during Axon Regeneration. Neuron. 2016;92(6):1294–307. [PubMed: 28009275]
46. Seong H-A, Jung H, Manoharan R, and Ha H. Positive regulation of apoptosis signal-regulating kinase 1 signaling by ZPR9 protein, a zinc finger protein. The Journal of Biological Chemistry. 2011;286(36):31123–35. [PubMed: 21771788]
47. Kim RH, Wang D, Tsang M, Martin J, Huff C, de Caestecker MP, et al. A novel Smad nuclear interacting protein, SNIP1, suppresses p300-dependent TGF-β signal transduction. Genes & Development. 2000;14(13):1605–16. [PubMed: 10887155]
48. Pan H, Qin K, Guo Z, Ma Y, April C, Gao X, et al. Negative elongation factor controls energy homeostasis in cardiomyocytes. Cell Reports. 2014;7(1):79–85. [PubMed: 24656816]
49. Bénit P, Chretien D, Kadhom N, de Lonlay-Debeney P, Cormier-Daire V, Cabral A, et al. Large-scale deletion and point mutations of the nuclear NDUFV1 and NDUFS1 genes in mitochondrial complex I deficiency. American Journal of Human Genetics. 2001;68(6):1344–52. [PubMed: 11349233]
50. Hui DY, and Howles PN. Carboxyl ester lipase. Journal of Lipid Research. 2002;43(12):2017–30. [PubMed: 12454261]
51. Su Q, Zhang P, Yu D, Wu Z, Li D, Shen F, et al. Upregulation of miR-93 and inhibition of LIMK1 improve ventricular remodeling and alleviate cardiac dysfunction in rats with chronic heart failure by inhibiting RhoA/ROCK signaling pathway activation. Aging. 2019;11(18):7570–86. [PubMed: 31541994]
52. Westermann D, Mersmann J, Melchior A, Freudenberger T, Petrik C, Schaefer L, et al. Biglycan Is Required for Adaptive Remodeling After Myocardial Infarction. Circulation. 2008;117(10):1269–76. [PubMed: 18299507]
53. Chen CY, Salomon AK, Caporizzo MA, Curry S, Kelly NA, Bedi K, et al. Depletion of Vasohibin 1 Speeds Contraction and Relaxation in Failing Human Cardiomyocytes. Circulation Research. 2020;127(2):e14–e27. [PubMed: 32272864]

54. Buijs RR, Hummel JJA, Burute M, Pan X, Cao Y, Stucchi R, et al. WDR47 protects neuronal microtubule minus ends from katanin-mediated severing. Cell Reports. 2021;36(2):109371. [PubMed: 34260930]
55. Robison P, Caporizzo MA, Ahmadzadeh H, Bogush AI, Chen CY, Margulies KB, et al. Detyrosinated microtubules buckle and bear load in contracting cardiomyocytes. Science. 2016;352(6284):aaf0659. [PubMed: 27102488]
56. Jong J, Pinney JR, and Packard RRS. Anthracycline-induced cardiotoxicity: From pathobiology to identification of molecular targets for nuclear imaging. Frontiers in Cardiovascular Medicine. 2022;9:919719–. [PubMed: 35990941]
57. Packard RRS. Cardiac fibrosis in oncologic therapies. Current Opinion in Physiology. 2022;29:100575. [PubMed: 36187050]
58. Vejpongsa P, and Yeh ETH. Prevention of Anthracycline-Induced Cardiotoxicity. Journal of the American College of Cardiology. 2014;64(9):938–45. [PubMed: 25169180]
59. Chen J, Ding Y, Chen M, Gau J, Jen N, Nahal C, et al. Displacement analysis of myocardial mechanical deformation (DIAMOND) reveals segmental susceptibility to doxorubicin-induced injury and regeneration. JCI Insight. 2019;4(8):e125362. [PubMed: 30996130]
60. Butt AJ, Fraley KA, Firth SM, and Baxter RC. IGF-Binding Protein-3-Induced Growth Inhibition and Apoptosis Do Not Require Cell Surface Binding and Nuclear Translocation in Human Breast Cancer Cells. Endocrinology. 2002;143(7):2693–9. [PubMed: 12072403]
61. Cobb LJ, Liu B, Lee K-W, and Cohen P. Phosphorylation by DNA-Dependent Protein Kinase Is Critical for Apoptosis Induction by Insulin-Like Growth Factor Binding Protein-3. Cancer Research. 2006;66(22):10878–84. [PubMed: 17108124]
62. Santer FdrR, Bacher N, Moser BMorandell D, Ressler S, Firth SM, et al. Nuclear Insulin-Like Growth Factor Binding Protein-3 Induces Apoptosis and Is Targeted to Ubiquitin/Proteasome–Dependent Proteolysis. Cancer Research. 2006;66(6):3024–33. [PubMed: 16540651]
63. Lin MZ, Marzec KA, Martin JL, and Baxter RC. The role of insulin-like growth factor binding protein-3 in the breast cancer cell response to DNA-damaging agents. Oncogene. 2012;33(1):85–96. [PubMed: 23178489]
64. de Silva HC, Lin MZ, Phillips L, Martin JL, and Baxter RC. IGFBP-3 interacts with NONO and SFPQ in PARP-dependent DNA damage repair in triple-negative breast cancer. Cellular and Molecular Life Sciences. 2019;76(10):2015–30. [PubMed: 30725116]
65. Nair AB, and Jacob S. A simple practice guide for dose conversion between animals and human. Journal of Basic and Clinical Pharmacy. 2016;7(2):27–31. [PubMed: 27057123]
66. Dhingra S, Sharma AK, Arora RC, Slezak J, and Singal PK. IL-10 attenuates TNF- -induced NF B pathway activation and cardiomyocyte apoptosis. Cardiovascular Research. 2009;82(1):59–66. [PubMed: 19181934]
67. Sun H, Olson KC, Gao C, Prosdocimo DA, Zhou M, Wang Z, et al. Catabolic Defect of Branched-Chain Amino Acids Promotes Heart Failure. Circulation. 2016;133(21):2038–49. [PubMed: 27059949]
68. Liu Y, Beyer A, and Aebersold R. On the Dependency of Cellular Protein Levels on mRNA Abundance. Cell. 2016;165(3):535–50. [PubMed: 27104977]
69. Schwanhäusser B, Busse D, Li N, Dittmar G, Schuchhardt J, Wolf J, et al. Global quantification of mammalian gene expression control. Nature. 2011;473(7347):337–42. [PubMed: 21593866]
70. Rabkin S, and Sunga P. The effect of doxorubicin (adriamycin) on cytoplasmic microtubule system in cardiac cells. Journal of Molecular and Cellular Cardiology. 1987;19(11):1073–83. [PubMed: 3325651]
71. Song R, Yang Y, Lei H, Wang G, Huang Y, Xue W, et al. HDAC6 inhibition protects cardiomyocytes against doxorubicin-induced acute damage by improving α-tubulin acetylation. Journal of Molecular and Cellular Cardiology. 2018;124:58–69. [PubMed: 30315806]
72. Schuldt M, Pei J, Harakalova M, Dorsch LM, Schlossarek S, Mokry M, et al. Proteomic and Functional Studies Reveal Detyrosinated Tubulin as Treatment Target in Sarcomere Mutation-Induced Hypertrophic Cardiomyopathy. Circulation Heart Failure. 2021;14(1):e007022–e. [PubMed: 33430602]

73. Butler A, Hoffman P, Smibert P, Papalexi E, and Satija R. Integrating single-cell transcriptomic data across different conditions, technologies, and species. Nature Biotechnology. 2018;36(5):411–20.

74. Kannan S, Miyamoto M, Zhu R, Lynott M, Guo J, Chen EZ, et al. Trajectory reconstruction identifies dysregulation of perinatal maturation programs in pluripotent stem cell-derived cardiomyocytes. Cell Reports. 2023;42(4):112330. [PubMed: 37014753]

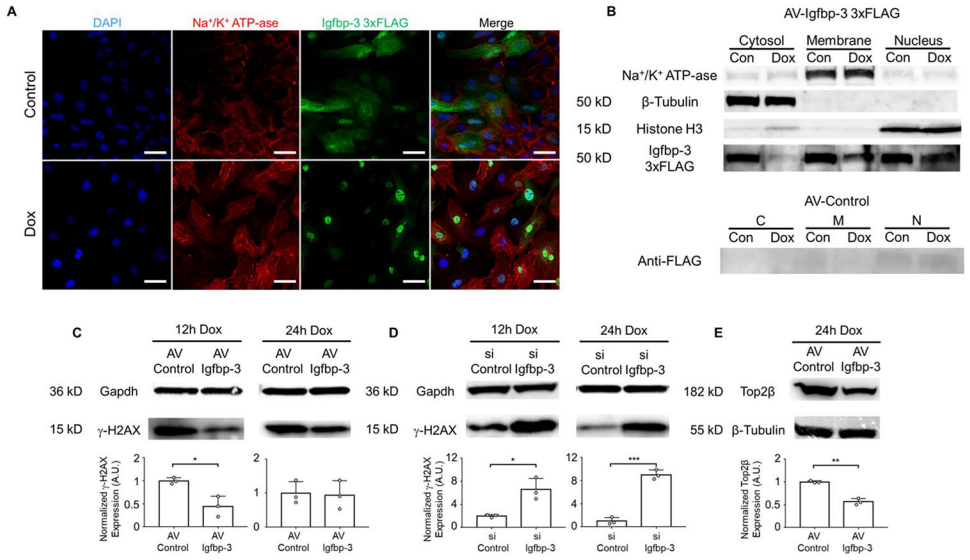


**Figure 1. Igfbp-3 is enriched in the nucleus and mitigates AIC.**

(A) Maximal projection confocal images indicating a decrease in cytoplasmic expression and a reciprocal increase in the nuclear fraction of Igfbp-3 after Dox treatment in NRVM. DAPI (blue) and $Na^+/K^+$ ATP-ase (red) staining of the nucleus and plasma membrane, respectively. Igfbp-3 3xFLAG staining in green. Objective: 63x. Scale bar: 20μm.

(B) Cell fractionation assay demonstrating decrease in the cytoplasmic fraction of 3xFLAG tagged Igfbp-3 detected by anti-FLAG antibody after Dox treatment in NRVM. $Na^+/K^+$ ATP-ase, β-tubulin, and histone H3 used as indicators for membrane, cytoplasm, and nuclear fractions, respectively.

(C-D) Phosphorylation of H2AX (γ-H2AX) in response to overexpression (C) or silencing (D) of Igfbp-3 under Dox treatment at 12h and 24h in NRVM, with Western blot semi-quantitation shown below the gels. AV: adenovirus overexpression, si: siRNA silencing. A.U.:arbitrary unit. N=3 biological replicates.

(E) Igfbp-3 overexpression is associated with a reduction in Top2β levels under Dox treatment in NVRM. N=3 biological replicates.

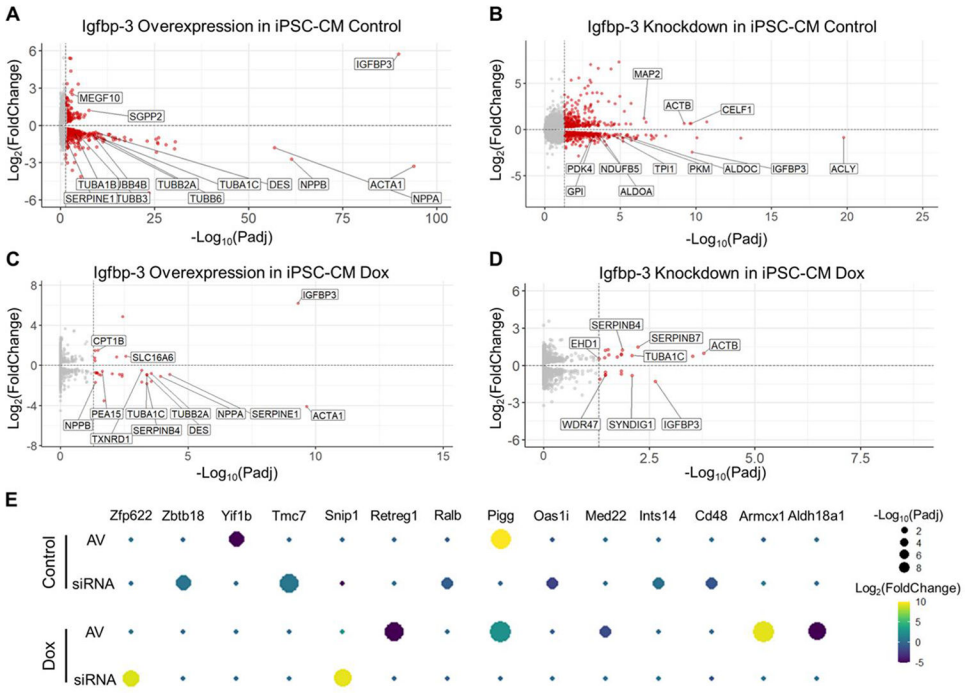


**Figure 2. Significantly regulated DEGs by Igfbp-3 manipulation in CM.**

(A-B) Volcano plots of DEGs in iPSC-CM when overexpressing Igfbp-3 (A) or silencing Igfbp-3 (B) under physiological condition. Significantly regulated genes are in red (cutoff threshold Padj<0.05). N=4 biological replicates.

(C-D) Volcano plots of DEGs in Dox treated iPSC-CM when overexpressing Igfbp-3 (C) or silencing Igfbp-3 (D). N=4 biological replicates.

(E) Significantly regulated DEGs by Igfbp-3 in NRVM. For each gene, Padj value is denoted by the size of the dot, and $Log_2$(FoldChange) is denoted by the color of the dot. N=3 biological replicates.

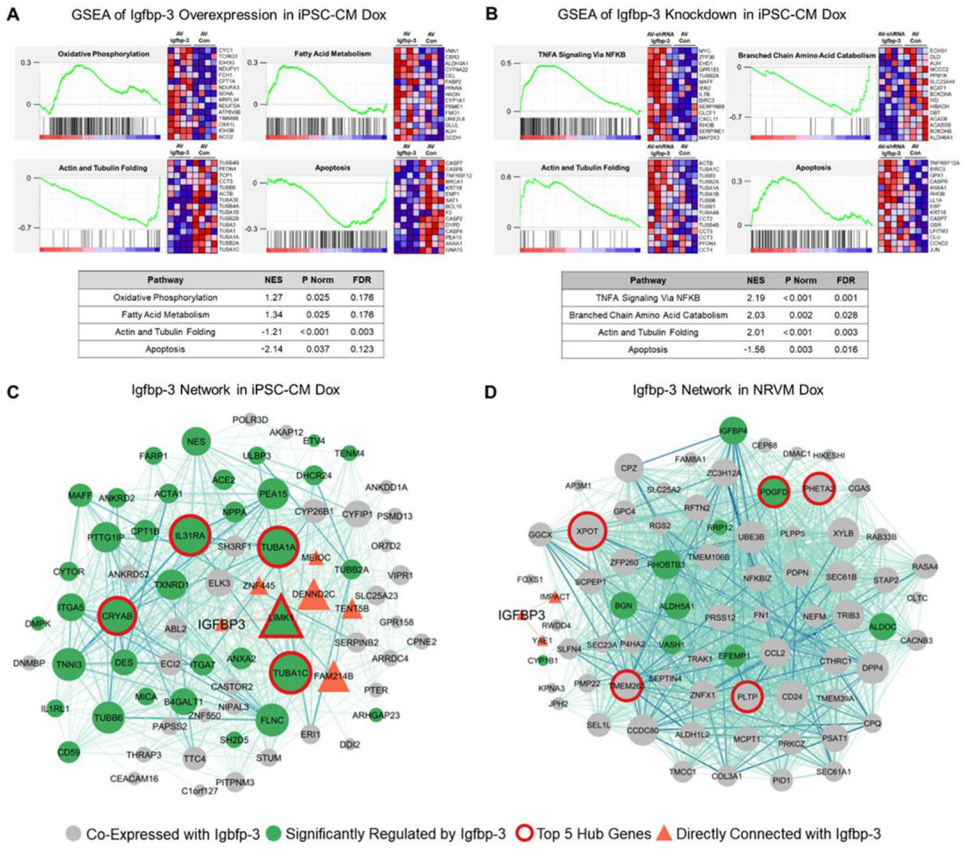


| Pathway | NES | P Norm | FDR |
|---|---|---|---|
| Oxidative Phosphorylation | 1.27 | 0.025 | 0.176 |
| Fatty Acid Metabolism | 1.34 | 0.025 | 0.176 |
| Actin and Tubulin Folding | -1.21 | <0.001 | 0.003 |
| Apoptosis | -2.14 | 0.037 | 0.123 |

| Pathway | NES | P Norm | FDR |
|---|---|---|---|
| TNFA Signaling Via NFKB | 2.19 | <0.001 | 0.001 |
| Branched Chain Amino Acid Catabolism | 2.03 | 0.002 | 0.028 |
| Actin and Tubulin Folding | 2.01 | <0.001 | 0.003 |
| Apoptosis | -1.56 | 0.003 | 0.016 |

**Figure 3. GSEA of perturbed pathways following Igfbp-3 modulation and WGCNA network construction.**

(A) GSEA of significantly altered pathways by Igfbp-3 overexpression in iPSC-CM after Dox treatment. Upregulated genes are denoted in red and downregulated genes in blue.

(B) GSEA of significantly altered pathways by Igfbp-3 silencing in iPSC-CM after Dox treatment.

(C) WGCNA network of genes co-expressed with Igfbp-3 under Dox treatment in iPSC-CM. Top 5 hub genes with the most connectivity with other network genes are highlighted with a red border, green genes are significantly perturbed by Igfbp-3 modulation in iPSC-CM, triangle genes are directly connected with Igfbp-3 in the network (i.e. their expression level highly correlates with Igfbp-3), and green triangle genes are significantly regulated by and directly connected with Igfbp-3.

(D) WGCNA network of genes co-expressed with Igfbp-3 under Dox treatment in NRVM. The network is annotated in the same way as the iPSC-CM network.

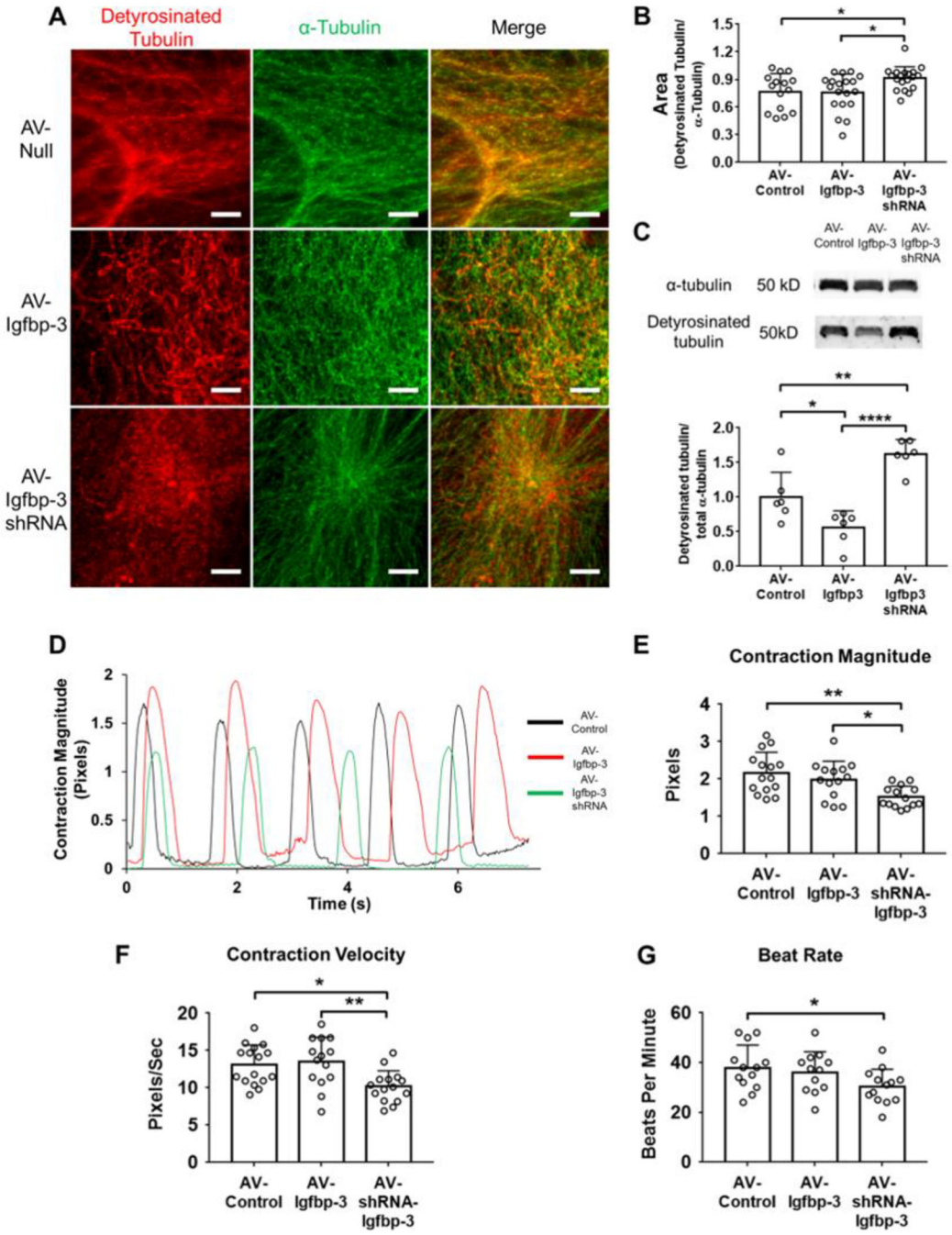


**Figure 4. Igfbp-3 interferes with detyrosinated microtubule accumulation and alters contractile function in Dox treated iPSC-CM.**

(A) Stimulated Emission Depletion (STED) microscopy images of iPSC-CM after Dox treatment. Red, detyrosinated tubulin. Green, total α-tubulin. Scale bar: 5μm. Objective: 100x.

(B) Quantification of detyrosinated tubulin area and total α-tubulin area ratio in STED images. Each dot represent one cell. Biological replicates: AV-Control n=16, AV-Igfbp-3 n=19, AV-Igbfp-3-shRNA n=19.

(C) Quantitative Western blot of detyrosinated tubulin and total α-tubulin ratio in iPSC-CM after Dox treatment. N=6 biological replicates.
(D-G) Under Dox treatment, Igfbp-3 silencing in iPSC-CM impedes contractile magnitude and velocity and decreases beat rate. N=14 biological replicates.

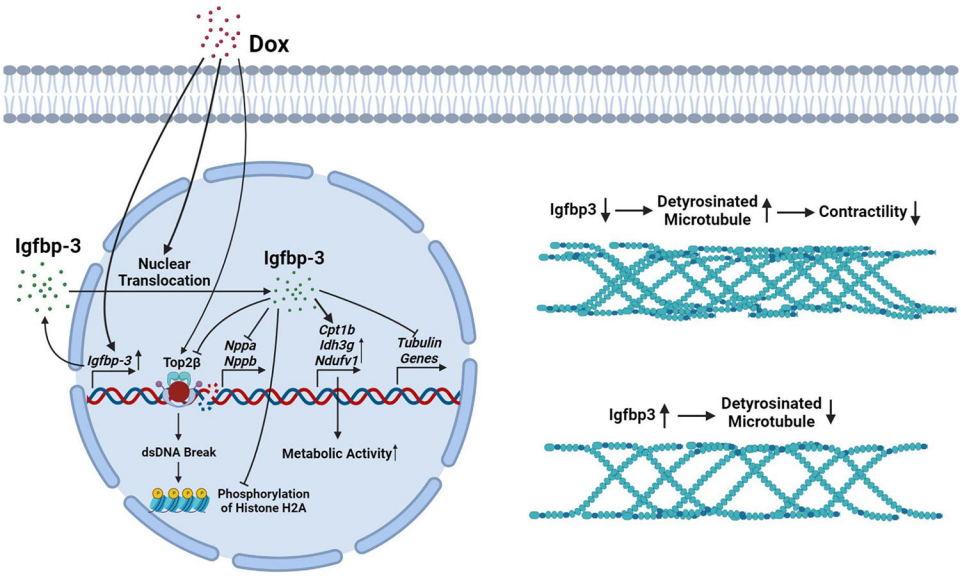


**Figure 5. Summary diagram depicting protective pathways controlled by Igfbp-3 in anthracycline-induced cardiomyocyte injury.**

Dox induces Igfbp-3 upregulation and nuclear translocation in cardiomyocytes. Igfpb-3 overexpression impedes Top2β expression and decreases Dox induced dsDNA break. In parallel, the heart failure markers *Nppa* and *Nppb* are significantly downregulated, while *Cpt1b, Idh3g,* and *Ndufv1*, which positively regulate cellular metabolic activity are significantly upregulated by Igfbp-3 overexpression. Functionally, Igfbp-3 knockdown leads to contractile dysfunction in iPSC-CM after Dox treatment, associated with upregulation of tubulin family genes and accumulation of detyrosinated tubulin.

## REAGENTS AND TOOLS TABLE

| REAGENT or RESOURCE | SOURCE | IDENTIFIER | RRID |
|---|---|---|---|
| **Antibodies** | | | |
| ANTI-FLAG® M2 antibody | Millipore Sigma | F1804 | AB_262044 |
| Anti Na+/K+ ATP-ase antibody | Abcam | ab76020 | AB_1310695 |
| Anti Igfbp-3 antibody (mouse,rat) | Abcam | ab220429 | |
| Anti Igfbp-3 antibody (human) | Abcam | ab193910 | |
| Anti-gamma H2A.X (phospho S139) antibody | Abcam | ab81299 | AB_1640564 |
| Anti-Topoisomerase II beta antibody | Abcam | ab109524 | AB_10859793 |
| Anti-alpha Tubulin antibody | Abcam | Ab7291 | AB_2241126 |
| Anti-Detyrosinated alpha Tubulin antibody | Abcam | ab48389 | AB_869990 |
| Anti-beta Tubulin antibody | Abcam | ab6046 | AB_2210370 |
| Anti-Histone H3 antibody | Abcam | ab1791 | AB_302613 |
| Anti-Gapdh antibody | Abcam | ab128915 | AB_11143050 |
| Rabbit IgG (H&L) Antibody ATTO 647N Conjugated | Rockland | 611-156-122 | AB_10893043 |
| Goat Anti-Mouse IgG H&L (Alexa Fluor® 594) | Abcam | ab150120 | AB_2631447 |
| Anti-Nppa antibody | Abcam | ab209232 | |
| Anti-Nppb antibody | ThermoFisher | PA5-96084 | |
| **Bacterial and virus strains** | | | |
| Ad-Null | Abmgood | 000048A | |
| Ad-rIgfbp3 | Abmgood | 2432305 | |
| Ad-hIgfbp-3 | Vector Biolabs | ADV-211932 | |
| Ad-hIgfbp-3-shRNA | Vector Biolabs | shADV-211932 | |
| **Chemicals, peptides, and recombinant proteins** | | | |
| Doxorubicin hydrochloride | Millipore Sigma | D1515 | |
| Gelatin Solution | Millipore Sigma | ES-006 | |
| Triton™ X-100 | Millipore Sigma | X100 | |
| DMEM | ThermoFisher | 10569010 | |
| RPMI1640 | ThermoFisher | 61870127 | |
| Fetal Bovine Serum | ThermoFisher | 10082147 | |
| B-27™ Supplement, minus insulin | ThermoFisher | A1895601 | |
| Lipofectamine™ RNAiMAX Transfection Reagent | ThermoFisher | 13778030 | |
| Insulin-Transferrin-Selenium (ITS-G) (100X) | ThermoFisher | 41400045 | |
| **Critical commercial assays** | | | |
| RNeasy Mini Kits | Qiagen | 74104 | |
| Cell Fractionation Kit | Abcam | ab109719 | |
| LDH release assay | Abcam | ab102526 | |
| TUNEL assay | ThermoFisher | C10619 | |

| REAGENT or RESOURCE | SOURCE | IDENTIFIER | RRID |
|---|---|---|---|
| MTT assay | Abcam | ab211091 | |
| SRB assay | Abcam | ab235935 | |
| **Deposited data** | | | |
| Raw and analyzed RNA-seq data | This paper | GSE206803 | |
| **Experimental models: Cell lines** | | | |
| Human induced pluripotent stem cell | UCLA | iPSC23 | |
| MDA-MB-231 cell line | ATCC | CRM-HTB-26 | CVCL_0062 |
| T47D cell line | ATCC | HTB-133 | CVCL_0553 |
| **Experimental models: Organisms/strains** | | | |
| C57Bl/6 mice | The Jackson Laboratory | 000664 | IMSR_JAX:000664 |
| **Oligonucleotides** | | | |
| Igfbp3 siRNA | Qiagen | SI00250866 | |
| **Software and algorithms** | | | |
| ImageJ | NIH | https://imagej.nih.gov/ij/ | SCR_003070 |
| DeSeq2 | Love et al., 2014 | R package | RRID:SCR_015687 |
| Seurat4.0 | Hao et al., 2021 | R package | RRID:SCR_016341 |
| Monocle3 | Qiu et al., 2017 | R package | RRID:SCR_018685 |
| Clustal Omega | Sievers et al, 2011 | https://www.ebi.ac.uk/Tools/msa/clustalo/ | SCR_001591 |
| Pulse Contractility | Maddah et al., 2015 | www.pulsevideoanalysis.com | |